Journal of Applied Physics

Strain-driven thermodynamic stability and electronic transitions in ZnX (X = O, S, Se, and Te) monolayers

Cite as: J. Appl. Phys. **125**, 082540 (2019); https://doi.org/10.1063/1.5053680
Submitted: 24 August 2018 . Accepted: 31 January 2019 . Published Online: 27 February 2019

Rajneesh Chaurasiya, Ambesh Dixit, and Ravindra Pandey

ARTICLES YOU MAY BE INTERESTED IN

Cooperative effects of strain and electron correlation in epitaxial VO_2 and NbO_2
Journal of Applied Physics **125**, 082539 (2019); https://doi.org/10.1063/1.5052636

Electrical contacts of coplanar 2H/1T′ $MoTe_2$ monolayer
Journal of Applied Physics **125**, 075104 (2019); https://doi.org/10.1063/1.5081936

Physics of picosecond pulse laser ablation
Journal of Applied Physics **125**, 085103 (2019); https://doi.org/10.1063/1.5080628

© 2019 Author(s).

Journal of Applied Physics | ARTICLE | scitation.org/journal/jap

Strain-driven thermodynamic stability and electronic transitions in ZnX (X = O, S, Se, and Te) monolayers

Cite as: J. Appl. Phys. **125**, 082540 (2019); doi: 10.1063/1.5053680
Submitted: 24 August 2018 · Accepted: 31 January 2019 ·
Published Online: 27 February 2019

View Online
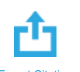
Export Citation

CrossMark

Rajneesh Chaurasiya,[1] Ambesh Dixit,[1,a)] and Ravindra Pandey[2]

AFFILIATIONS

[1]Department of Physics and Center for Solar Energy, Indian Institute of Technology Jodhpur, Jodhpur, Rajasthan 342037, India
[2]Department of Physics, Michigan Technological University, Houghton, Michigan 49931, USA

[a)]ambesh@iitj.ac.in

ABSTRACT

Semiconducting Zn chalcogenide monolayers are important members of the 2D family of materials due to their unique electronic properties. In this paper, we focus on strain-modulated electronic properties of monolayers of ZnX, with X being O, S, Se, and Te. ZnO and ZnS monolayers have a hexagonal graphene-like planar structure, while ZnSe and ZnTe monolayers exhibit slightly buckled silicene and germanene-like structures, respectively. Density functional theory calculations find the hexagonal ZnO monolayer to be dynamically stable. However, ZnS, ZnSe, and ZnTe monolayers are predicted to be less stable with small imaginary frequencies. The application of tensile strain to these monolayers, interestingly, yields stability of dynamically less stable structures together with the modification in the nature of the bandgap from direct to indirect. For a tensile strain of about 8%, a closure of the bandgap in ZnTe is predicted with the semiconductor-metal transition. The results, therefore, find strain-induced stability and modification in electronic properties of monolayers of Zn chalcogenides, suggesting the use of these monolayers for novel device applications.

Published under license by AIP Publishing. https://doi.org/10.1063/1.5053680

I. INTRODUCTION

2D monolayers and their derivatives such as nanoribbons have attracted attention due to their potential in electronic and optoelectronic applications.[1–5] Graphene is one of the most studied 2D materials due to its unique physical and electronic properties. However, the absence of the bandgap limits its potential for nanoscale electronic devices.[6] This has, therefore, motivated several researchers to explore alternative 2D materials with finite bandgaps. One of the examples of such 2D materials is a family of transition metal dichalcogenides.[7–14] In this paper, we focus on monolayers of zinc chalcogenides, which have previously been investigated. For example, monolayers of ZnX, with X being O, S, Se, and Te, are predicted to be direct bandgap semiconductors.[9] The synthesis of ZnO honeycomb layered monolayer has been reported.[15,16] Likewise, a heteroepitaxial growth of the ZnO monolayer on graphene using the atomic layer deposition method was reported[17] with a measured bandgap of 4.0 eV. ZnS nanosheets with a width of ~11 Å were synthesized in the wurtzite phase using the hydrothermal method with a bandgap of 5.08 eV.[18] Theoretical studies[19–29] based on the density functional theory reported the ZnO monolayer to be stable, while ZnS, ZnSe, and ZnTe monolayers are predicted to be thermodynamically less stable.

The physical and chemical properties of nanomaterials can be modulated by strain in nanosystems, leading to thermodynamic stability and respective changes in their properties.[30–32] In general, strain engineering and the application of an external electric field are employed[33] to tailor the properties of 2D materials. The effect of strain on the electronic properties of 2D materials, especially graphene, has been extensively investigated.[34–37] In this paper, we focus on the strain engineering of the properties of ZnX monolayers to see if the strained monolayers can be stable.

As a practical issue, strain is almost inevitable in fabricated monolayer nanostructures, manifesting as the formation

Published under license by AIP Publishing.

of ridges and buckling. The strain in 2D materials can be introduced in many ways such as depositing them onto the flexible substrate, by subjecting them to the external load, by pseudomorphic growth, and by nanoindentation of the system. In particular, graphene and MoS_2 possess superior mechanical flexibility and can sustain a spectacularly large strain (<25%).[38,39] We will consider both tensile and compressive strains, and each type of strain can be applied along the biaxial direction in the chalcogenide monolayers.

II. COMPUTATIONAL METHOD

Initially, a wurtzite structure with Zn atoms surrounded by chalcogens is considered in the tetrahedral symmetry, which consists of two formula units in a unit cell. After removing one formula unit from the ZnX unit cell orthogonally to $\vec{a_3}^{3D} \equiv$ c lattice parameter, 2D monolayers of ZnX systems are constructed, exhibiting half of the symmetry operators with respect to that of the bulk.[40] A hexagonal supercell (4 × 4) of the ZnX monolayer in conjunction with 15 Å vacuum along the z-axis to avoid the interlayer interaction was considered. Structural optimization was performed using the density functional theory (DFT) as implemented in the SIESTA code.[41–44] The generalized gradient approximation with the Perdew Burke Ernzerhoff (GGA-PBE)[45] type parameterization was employed. Troullier-Mertin non-conserving pseudo-potentials were used, factorized under the Kleinman and Bylander scheme. The valence electrons were described by the localized pseudo-atomic orbitals (PAOs), with the double-ζ double polarized basis sets.[46] The structural optimization was carried out using force and stress convergence criteria of 0.001 eV/Å and 0.001 eV/Å^3, respectively. A large plane wave mesh cutoff of 150 Ry was used. The K-point sampling of 10 × 10 × 1 was used for the structural optimization, and the 20 × 20 × 1 sampling was used for the band structure and density of states calculations in conjunction with a 75 Ry mesh cutoff for the real space grid sampling. The dynamical stability of these monolayers is investigated using the density functional perturbation theory (DFPT) as implemented in PWSCF-Quantum Espresso (QE).[47,48] Here, we used the ultrasoft pseudopotentials under GGA in conjunction with the PBE exchange and the correlation functional form. The kinetic energy cutoff was set at 30 Ry and 12 × 12 × 1 K-point sampling was considered using the Monkhorst-Pack scheme[49] for calculations for optimization. We used the 8 × 8 × 1 K-point sampling for optimization and self-consistent field (SCF) calculation. The biaxial strain in both tensile and compressive modes along the xy direction was defined as $\epsilon(\%) = (a - a_0)/a_0$, where a and a_0 are lattice parameters for the strained and pristine systems, respectively.

III. RESULT AND DISCUSSIONS

Figure 1 shows top and side views of ZnX hexagonal monolayers. Here, Δd is the buckling parameter and d is the bond length. In the equilibrium configuration, the lattice parameters are 3.32 Å, 3.87 Å, 4.06 Å, and 4.40 Å for ZnO, ZnS, ZnSe, and ZnTe monolayers, respectively. These values are compared with the previously reported values as listed in Table I. Note that a planar graphene-like structure is predicted for ZnO and ZnS monolayers, substantiating sp^2 hybridization between Zn-O (S) atoms. A 15 Å vacuum along the z direction in ZnO and ZnS monolayers avoids the interaction of atoms with top most electrons and also the interaction of p_z orbital of Zn and O(S) atom is not dominating. That is why ZnO and ZnS form the planar structure.[50] Further, with increasing size of the chalcogen elements, interaction of the p_z orbital of Zn with Se(Te) atoms is significant, causing the low buckling in ZnSe and ZnTe monolayers, similar to that of silicene and germane, suggesting sp^3 hybridization between Zn-Se(Te) atoms in the 2D lattice.[51] The buckling parameters are 0.31 Å and 0.35 Å for ZnSe and ZnTe monolayers, respectively. The lattice parameters and buckling value of ZnSe and ZnTe differ slightly from the work of Zheng *et al.*[9] using the local density approximation (LDA). In contrast, the lattice parameters are nearly identical with the work of Safari *et al.*[51] using GGA-PBE exchange correlation potentials.

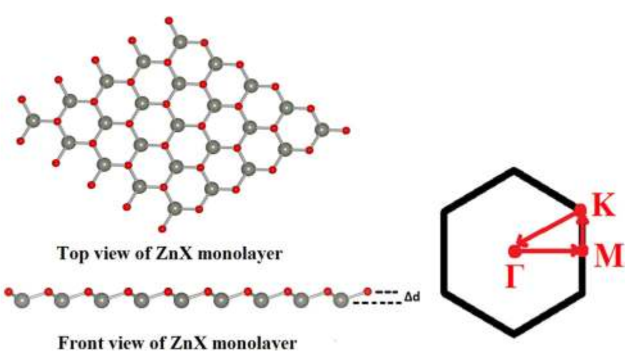

FIG. 1. Schematic diagram for a hexagonal ZnX monolayer, with X being O, S, Se, and Te. Δd represents buckling in the monolayer. The reciprocal space with high symmetry points is also displayed. (Gray spheres represent zinc atoms and red spheres represent chalcogen atoms.)

The cohesive energy, E_C, can be computed by taking the difference between the total energy of the system and the atomic constituents as $E_C = E_{ZnX} - E_{Zn} - E_X$, where E_{ZnX} is the total energy of ZnX unit cell, E_{Zn} and E_X are the total energies for zinc and X (O, S, Se, and Te) atoms, respectively. The calculated cohesive energies are 9.4 eV, 7.6 eV, 6.1 eV, and 5.3 eV for ZnO, ZnS, ZnSe, and ZnTe monolayers, respectively. The cohesive energy value is the maximum for the ZnO monolayer substantiating the strongest bonding between the Zn–O atoms. Note that Zn–X bond strength decreases in the order of ZnO > ZnS > ZnSe > ZnTe. Our results are in agreement with the work of Zheng *et al.* based on LDA calculations.[9] The trend in cohesive energy is also reflected in the computed electron difference density (EDD) plots as shown in Fig. 2. The electronegativity values of Zn and O atoms confirm the ionic and small covalent character, as evident from the EDD contour plot for the ZnO monolayer showing transfer of electron from Zn to O atom in the lattice. The EDD for other Zn-X

Published under license by AIP Publishing.

TABLE I. Calculated structural and electronic properties of ZnX (with X = O, S, Se, and Te) monolayers.

	ZnO		ZnS		ZnSe		ZnTe	
Properties	This work	Previously reported	This work	Previously reported	This work	Previously reported	This work	Previously reported
Lattice parameter (Å)	3.32	3.23,[a] 3.21[b]	3.87	3.80,[b] 3.89,[c] 3.88[d]	4.06	3.99,[b] 4.10[d]	4.40	4.29,[b] 4.43[d]
Bond length (Å)	1.91	1.90,[e] 1.866,[a] 1.85,[b] 1.91,[f] 1.92,[g] 1.90[h]	2.23	2.19,[b] 2.25[c]	2.40	2.31[b]	2.59	2.5[b]
Bond angle (degree)	120	120.03[e]	120	120,[b] 120[c]	117.1		116.0	
Buckling value (Å)	0	0	0	0	0.31	0.18[b]	0.35	0.37[b]
Cohesive energy (eV)	9.43	8.38[b]	7.65	6.68[b]	6.09	5.95[b]	5.34	5.17[b]
Bandgap (eV)	1.83	1.65,[e] 2.03,[a] 1.66,[h] 1.68,[b] 4.0[i]	2.8	2.66,[b] 2.77,[j] 2.65,[k] 5.08[l]	1.84	1.92 eV[b]	1.37	1.73[b]

[a]Reference 19.
[b]Reference 9.
[c]Reference 24.
[d]Reference 46.
[e]Reference 22.
[f]Reference 21.
[g]Reference 15.
[h]Reference 20.
[i]Reference 16.
[j]Reference 23.
[k]Reference 25.
[l]Reference 17.

monolayers is summarized in Fig. 2. The electronegativity of the anion is decreasing from S to Se to Te, substantiating the covalent nature and is in agreement with observed EDD contour plots [Figs. 2(b)–2(d)]. Safari *et al.*[51] reported similar observations for ZnS, ZnSe, and ZnTe monolayers. The effective charge sharing is increasing from O to S to Se to Te, as can be seen in respective EDD contour plots (Fig. 2).

To determine the dynamic stability of ZnX monolayers, the phonon band dispersions were computed along the high symmetry points Γ-M-K-Γ of the Brillouin zone using the DFPT inbuilt in the QE code. The respective dispersion curves are shown in Fig. 3, exhibiting six phonon modes. The lowest three are acoustic phonon modes and the rest three are optical phonon modes. Acoustic modes are expressed as ZA, TA, and LA; and optical modes as ZO, TO, and LO, where Z stands for out of plane vibration along the vacuum region, A stands for acoustic, O for optical, T for transverse, and L for longitudinal modes. ZnO phonon dispersion curve [Fig. 3(a)] is showing the dynamical stability of the ZnO monolayer, as the calculated frequencies are real across the Brillouin zone. The frequency of the ZO optical mode is closer to acoustic phonon modes with a separation of 220 cm^{-1} energy gap between LA and TO vibrational modes for the ZnO monolayer. TO/LO optical phonon modes are degenerate at Γ for ZnO, ZnS, ZnSe, and ZnTe monolayers with values of 481, 365, 247, and 199 cm^{-1}, respectively. The magnitude of the optical and acoustic branch depends on the mass of atoms present in the unit cell. There is a significant reduction in degenerate TO/LO modes at Γ from ZnO to ZnTe systems as the mass of the anion (i.e., chalcogen atom) is increasing from O to S to Se to Te atoms. These degenerate TO/LO bands are similar to those calculated in the graphite phonon dispersion curve.[52] The energy of the ZO phonon mode, out of plane optical vibration mode, is very close to the acoustic modes of the ZnO monolayer, similar to that of the graphite system.[52] This energy separation becomes larger for ZnSe and ZnTe, similar to that calculated for the phonon band dispersion of low buckled germanene and silicene monolayers.[53] The frequency dispersion becomes imaginary for the ZnS monolayer, where the ZA phonon branch showed imaginary frequency dispersion [Fig. 3(b)] along the M-K direction. The onset of such imaginary frequencies substantiates that ZnS is less dynamically stable. Furthermore, ZA phonon dispersion in low buckled ZnSe and ZnTe monolayers also showed relatively small imaginary frequencies (<8 cm^{-1}) at Γ in ZnSe and at Γ and along the M-K direction for the ZnTe monolayer. These hexagonal monolayers seem to be relatively less stable with respect to the ZnS monolayer.

The calculated band structure along Γ-M-K-Γ and density of states (DOS) for these monolayers are shown in Figs. 4–7 in conjunction with the respective total and partial DOS. The direct bandgap of the ZnO monolayer is 1.83 eV at Γ, which is in agreement with the previously reported literature, as listed in Table I. The computed bandgap is less than the experimentally synthesized ZnO monolayer bandgap of 4.0 eV by Hong *et al.*[54] and is attributed to the GGA-PBE exchange correlation functional, which is prone to underestimate the bandgap of semiconductor materials. No significant change in carriers' effective mass along K-M is expected, whereas along other directions, carriers' effective mass should change depending on the slope of the parabolic section of the band. The computed effective masses of electrons are $0.24m_e$ and

Published under license by AIP Publishing.

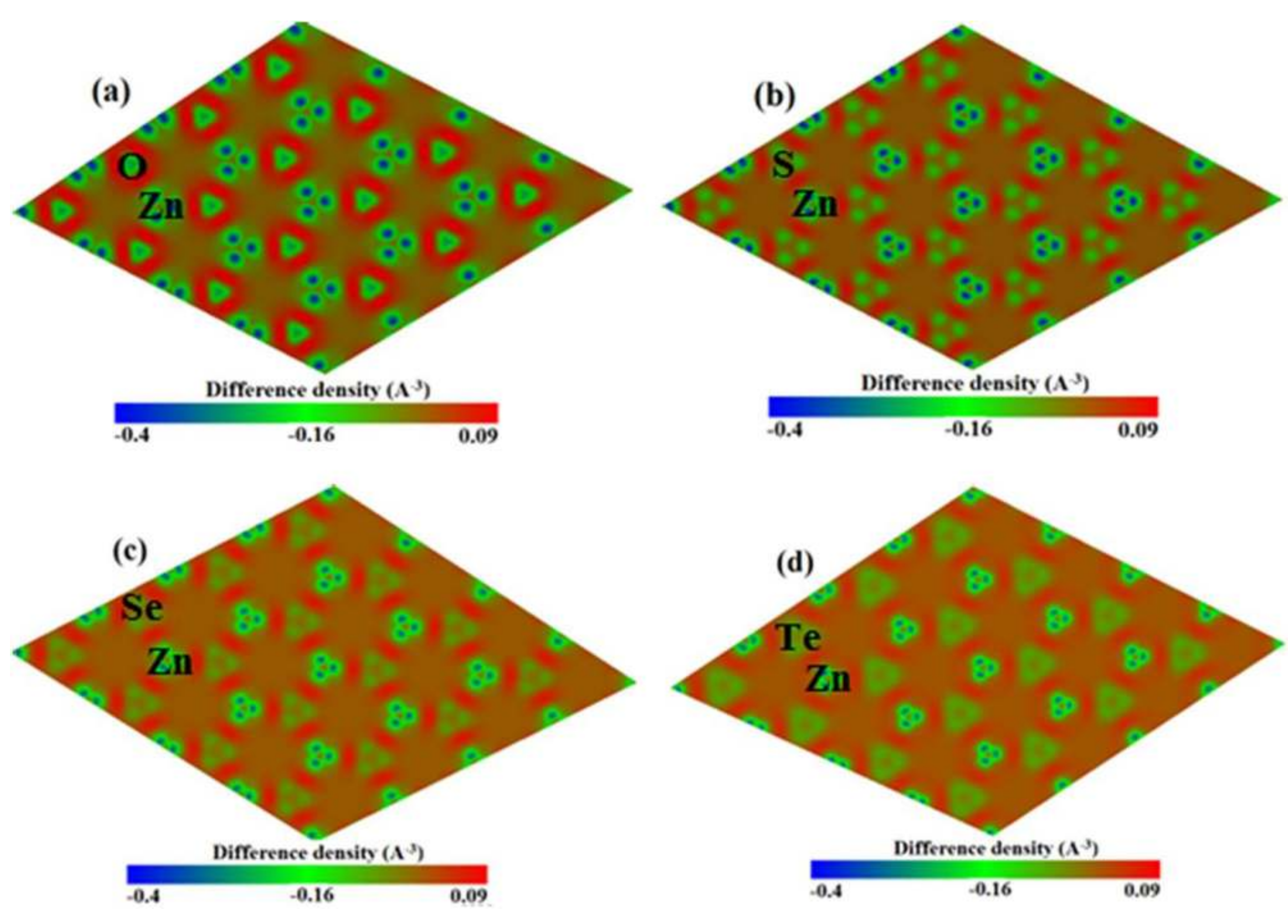

FIG. 2. Contour plots of electron difference density (i.e., difference in the number of electrons per unit volume) of (a) ZnO, (b) ZnS, (c) ZnSe, and (d) ZnTe monolayers. Negative values represent the charge accumulation, and positive values represent the charge depletion in the lattice.

$0.24m_e$ along (100) and (110) directions, respectively, and the effective masses of holes are $0.57m_e$ and $1.00m_e$ along (100) and (110) directions, respectively. These carrier effective mass values are similar to the values reported by Behara and Mukhopadhyay[36] based on the full-potential (linearized) augmented plane wave plus the local orbital (FP-(L)APW+lo) method.

The band structure of the ZnS monolayer is plotted in Fig. 5(a), showing it to be a direct bandgap semiconductor with a bandgap of 2.8 eV. The computed bandgap is consistent with the report of Lashgari *et al.*[24] but less than the experimental reported bandgap of 5.08 eV of ultra-thin ZnS nanosheets.[18] The band dispersions near conduction band minima (CBM) are similar to the ZnO monolayer, i.e., a large variation is observed along Γ-M and K-Γ with a little dispersion along K-M. The band dispersions near valence band maxima (VBM) are almost similar to that of CBM. The computed effective masses of electrons are $0.16m_e$ and $0.16m_e$ and that of holes are $0.37m_e$ and $0.66m_e$ along (100) and (110), respectively, for the ZnS monolayer.

The band structure of the buckled ZnSe monolayer is shown in Fig. 6(a), showing the direct bandgap at Γ with a bandgap of 1.84 eV, consistent with the work of Zheng *et al.*.[9] The band dispersion near CBM is similar to that of ZnO and ZnS monolayers, showing large dispersions along Γ-M and K-Γ and a small variation along M-K. The effective masses of conduction band electrons are $0.11m_e$ and $0.11m_e$ along (100) and (110) directions, respectively, and that of holes in valence band are $0.31m_e$ and $0.68m_e$ along (100) and (110) directions, respectively. The ZnTe monolayer also shows buckling similar to that of the ZnSe monolayer and the band structure is shown in Fig. 7(a). The band structure is similar to that of the ZnSe monolayer, showing a direct bandgap of 1.37 eV at Γ [Fig. 7(a)]. The band dispersions are showing similar variations and the computed conduction band electron effective masses are $0.08m_e$ and $0.08m_e$ and the valence band hole effective masses are $0.25m_e$ and $0.60m_e$ along (100) and (110) directions, respectively.

The effective masses of electrons are nearly same along (100) and (110) directions for these monolayers. In contrast,

Published under license by AIP Publishing.

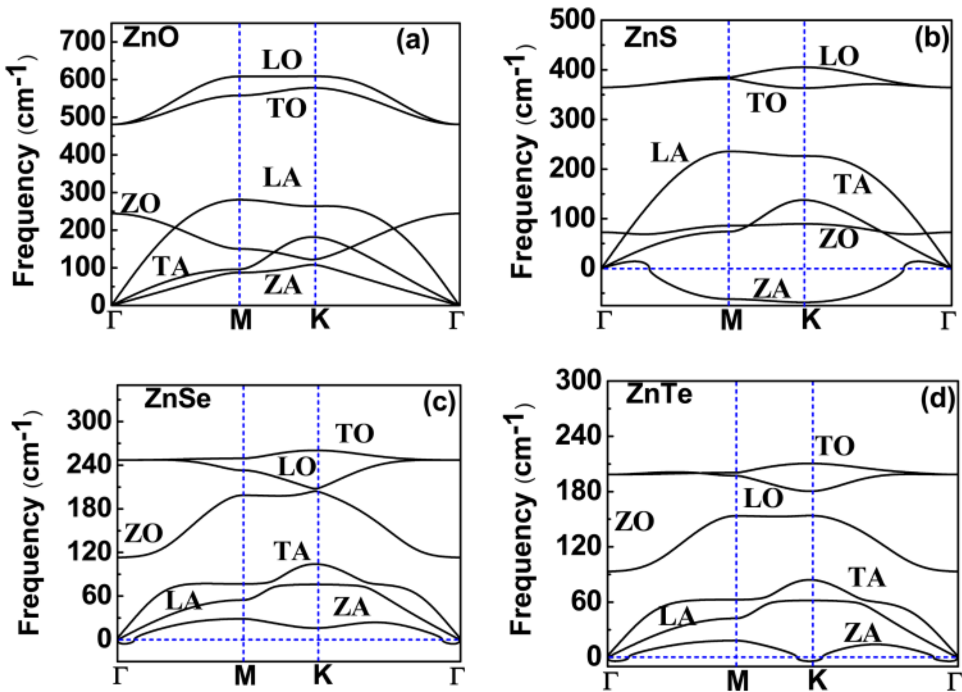

FIG. 3. Calculated phonon band dispersion curves for (a) ZnO, (b) ZnS, (c) ZnSe, and (d) ZnTe monolayers.

the hole effective masses are relatively sensitive to the respective directions. The effective mass of holes along the (110) direction is approximately two times that of the (100) direction. The observed variation in the hole effective mass values is attributed to the narrower parabolic region along (110) near VBM with respect to the (100) direction.

We also computed the partial density of states (PDOS) in the interval of −4 to 4 eV and they are plotted next to the respective band structures in Figs. 4–7. The PDOS of the ZnO monolayer suggests that the valence band near the Fermi level is mainly dominated by O-p states in conjunction with significant contributions from Zn-p and Zn-d states. This suggests a strong hybridization between Zn and O atoms in the lattice. The conduction band of the ZnO monolayer is dominated by Zn-s states in conjunction with a small contribution from Zn-p and O-p states. The ZnS monolayer PDOS [Fig. 5(b)] is similar to the planar ZnO monolayer [Fig. 4(b)]. Here, the CBM are mostly filled with Zn-s and S-p orbitals and the deep conduction region is dominated by Zn-p orbitals, which is also more localized around ~3.1 eV. The VBM near the Fermi energy is mostly contributed by S-p orbitals in conjunction with a small contribution from Zn-p and Zn-d orbitals.

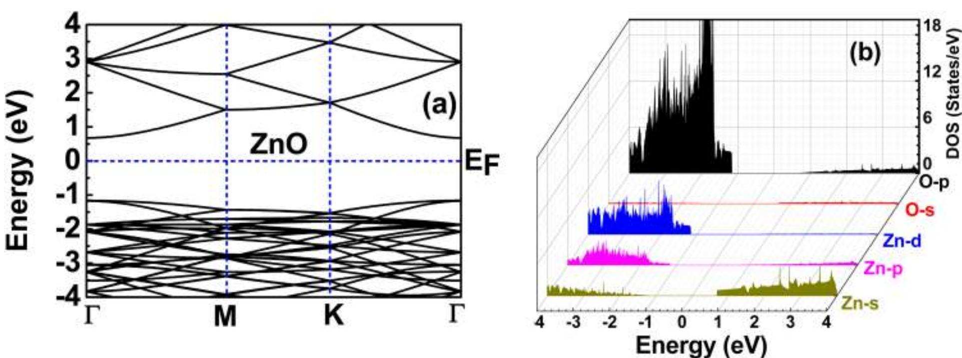

FIG. 4. (a) Band structure and (b) partial density of states of the ZnO monolayer.

Published under license by AIP Publishing.

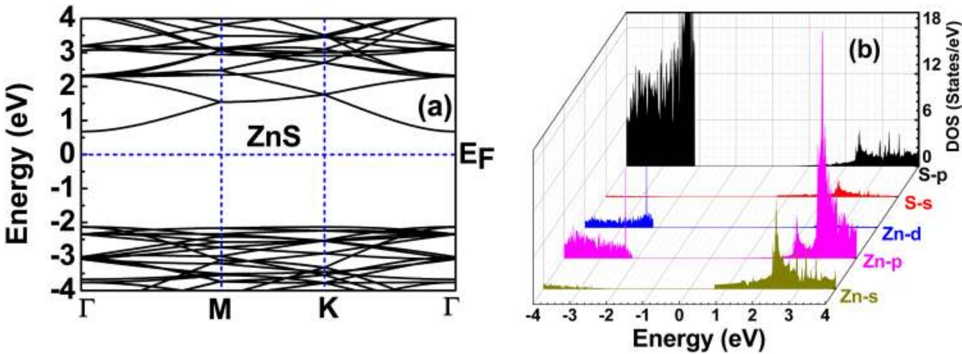

FIG. 5. (a) Band structure and (b) partial density of states of the ZnS monolayer.

Figure 6(b) shows PDOS of the buckled ZnSe monolayer, in which the states near the VBM are mostly dominated by Se-p states in conjunction with Zn-p and Zn-s orbitals near the Fermi energy. The region near CBM is showing a major contribution from Zn-s states with a small contribution from Zn-p and Se-p states. Zn-d states contribute in the deeper region of the conduction band. In contrast, Zn-s and Zn-p states constituting conduction bands are dispersive, suggesting the delocalization of s and p electrons in the lattice. A similar observation is also noticed for the buckled ZnTe monolayer [Fig. 7(b)]. The region near CBM is mainly dominated by Te-p (Se-p) and Zn-s states in the ZnTe (ZnSe) monolayer. Additionally, the highly localized Te-p states are also contributing deeper in the conduction band region. The region near VBM is dominated by Te-p (Se-p) and Zn-p states for ZnTe (ZnSe) monolayers, showing hybridization for these states in the lattice.

A. Strain-modulated structural properties

Considering strain as an important engineering parameter, we now investigate the impact of strain on these monolayer systems using both compressive and tensile strains (−8% to +8%) biaxially at an interval of 2%. The strain energy is defined as $E_S - E_P$, where E_S and E_P are the total energy of strained and pristine, i.e., pristine ZnX monolayers, respectively. The computed strain energy against biaxial strain is shown in Fig. 8, suggesting that the strain energy increases monotonously for both compressive and tensile strains. The impact of strain is investigated in terms of the bond length and buckling parameter for these ZnX monolayers. The variation in the bond length against strain is summarized in Fig. 9(a). This variation, i.e., change in the bond length shows linear enhancement or reduction for planar ZnO and ZnS monolayers and non-linear enhancement or reduction for buckled ZnSe and ZnTe monolayers after applying tensile or compressive strains [Fig. 9(a)]. The buckling height is also an important parameter to characterize the corrugation of the buckled 2D materials.[53,55–59] This is optimized for the buckled ZnSe and ZnTe structures against strain and computed optimized buckling is shown in Fig. 9(b). The maximum buckling for ZnSe and ZnTe monolayers was observed at −8% compressive strain confirming the strong sp^3 hybridization. This buckling decreases linearly from compressive to tensile strain and almost planar

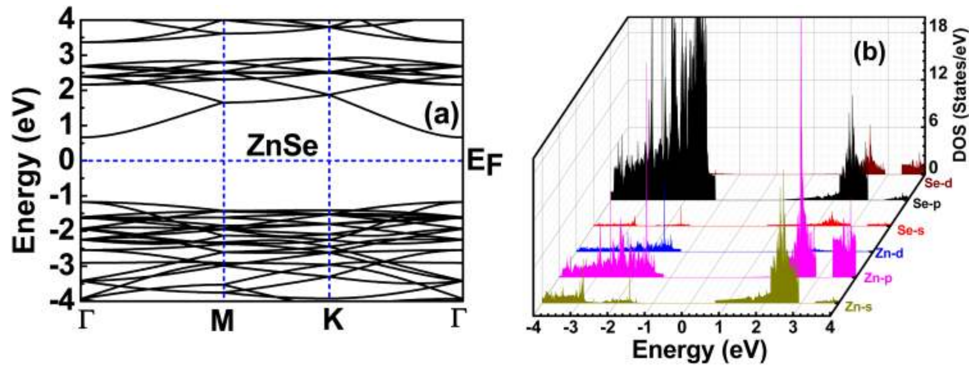

FIG. 6. (a) Band structure and (b) partial density of states of the ZnSe monolayer.

Published under license by AIP Publishing.

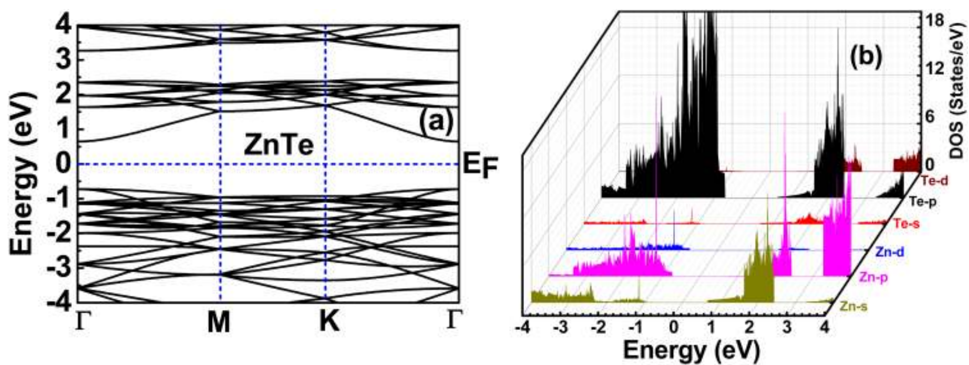

FIG. 7. (a) Band structure and (b) partial density of states of the ZnTe monolayer.

structures are observed at +8% of the tensile strain for both ZnSe and ZnTe monolayers, reducing buckling to approximately zero. Under the compressive strain, the interaction of p_z orbitals of Zn with Se (Te) has increased due to reduced bond lengths, which is why sp^3 hybridization is dominating. Moreover, in tensile strain, the interaction of Zn p_z orbitals with Se(Te) has reduced due to the increased bond length, which is why sp^3 hybridization gets weaker and buckling almost vanishes in ZnSe(Te) monolayers.

B. Strain-modulated phonon properties

The pristine ZnO monolayer is dynamically stable, as substantiated by the phonon dispersion curve [Fig. 3(a)] whereas buckled ZnSe and ZnTe pristine monolayers are less dynamically stable [Figs. 3(c) and 3(d)]. The pristine ZnS monolayer is also less dynamically stable, yet the calculated imaginary frequencies are small, suggesting it to be relatively less unstable [Fig. 3(b)], as compared to buckled ZnSe and ZnTe monolayers. To understand the impact of strain on their relative dynamic stability, we computed phonon dispersion curves for strained

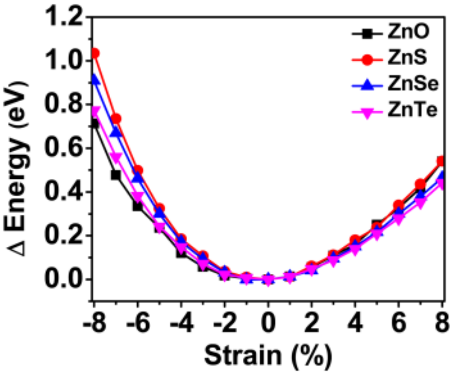

FIG. 8. Relative change in energy versus applied strain for different ZnX monolayers.

ZnX monolayers. The computed phonon dispersion curves at 2% and 6% strain are shown in Figs. 10–13 for ZnO, ZnS, ZnSe, and ZnTe monolayers under both compressive and tensile strains in conjunction with respective phonon spectra of the pristine monolayer. Phonon dispersion curves for 4% and 8% strain under compressive and tensile strains for ZnO, ZnS, ZnSe, and ZnTe monolayers are shown in the supplementary material (Figs. S1–S4).

We note that the ZnO monolayer can withstand the compressive strain up to −2% without losing its thermodynamic stability, whereas with a further increase in the compressive strain led to the onset of imaginary frequencies, showing a transition from dynamic stability to dynamic instability phase. The out of plane ZA acoustic vibrational mode showed softening with an increase in the compressive strain and became imaginary after −2% comprehensive strain (Fig. 10). The optical modes in ZnO monolayers also showed softening and out of plane ZO optical mode at −8% compressive strain, showing dynamic instability of the ZnO monolayer against compressive strains. Theoretically, degenerate LO/TO modes at Γ showed phonon hardening, i.e., shifting toward a higher frequency with an increase in the compressive strain. Sa *et al.*[60] also observed similar behavior in the phosphorene monolayer under the compressive strain. The splitting of LO/TO at M point decreases with an increase in the compressive strain and these modes become almost degenerate at −8% compressive strain shown in the supplementary material (Fig. S1), whereas the splitting of these LO/TO modes showed enhancement at K point with compressive strains.

In contrast to the compressive strain, the tensile strain showed an opposite impact on the ZnO monolayer. The out-of-plane acoustic mode ZA showed phonon hardening, whereas degenerate LO/TO optical modes at Γ showed phonon softening, i.e., reduced in frequency with an increase in the tensile strain. Jha and Soni[61] showed similar observations in the boron pnictide monolayer under tensile strains. The optical mode ZO (out of plane) gets degenerated with LO/TO modes at Γ for 8% tensile strain. The splitting of LO/TO modes at the M point enhanced with an increase in the tensile strain, whereas reduced at K with an increase in the tensile strain and became

Published under license by AIP Publishing.

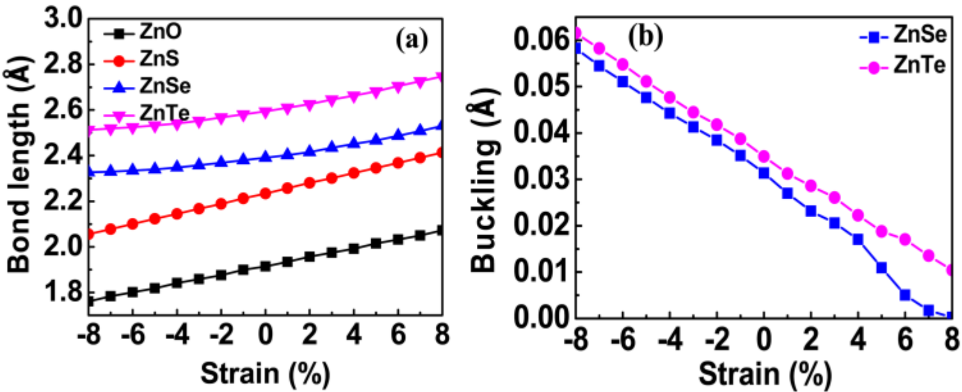

FIG. 9. (a) Bond length and (b) buckling height against strain for these monolayers (ZnO and ZnS monolayers are planar, which is why no buckling is computed for these systems).

almost degenerate at 8% tensile strain. Thus, the ZnO monolayer seems to be robust against tensile strain as the layer is dynamically stable upto such high 8% tensile strain.

The pristine ZnS monolayer is less dynamically stable as compared to the ZnO monolayer, and the ZA mode exhibits an imaginary frequency along the M-K direction. The ZnS monolayer is relatively more sensitive to the compressive strain, where the imaginary frequency of ZA mode increases with an increase in the compressive strain. The ZO phonon mode in the ZnS monolayer also lowered toward an imaginary frequency, making ZnS more unstable under compressive strain. The splitting of TO/LO modes at M and K increases with an increase in the compressive strain. The change in frequency for these modes is opposite for tensile strain. The out-of-plane ZA mode shows an increase in frequency, i.e., shifted toward positive frequency under tensile strains.

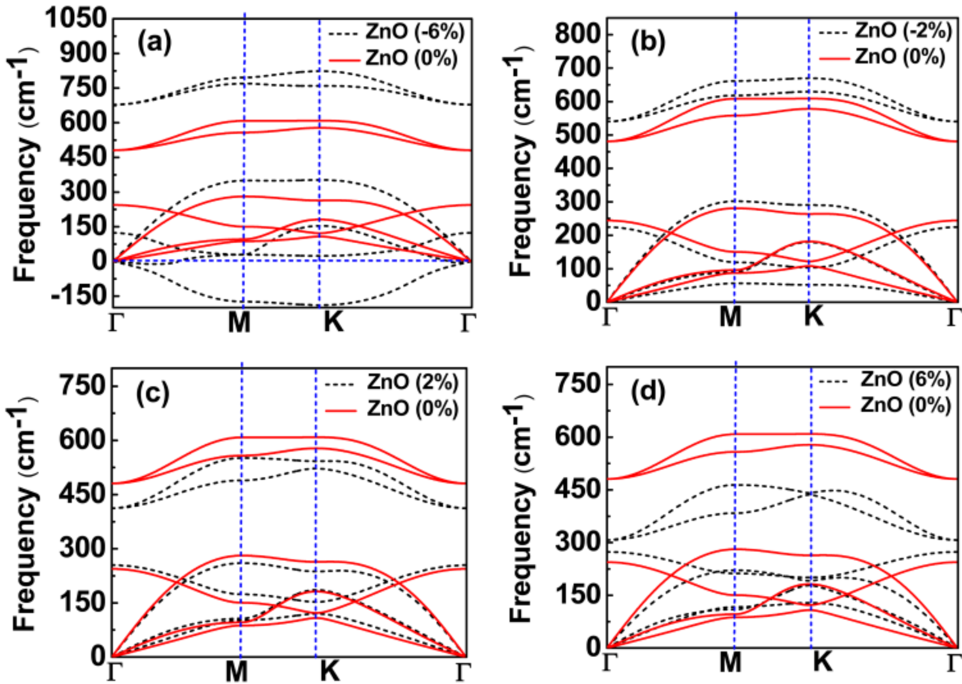

FIG. 10. Calculated phonon band dispersion of the ZnO monolayer: (a) 6% compression strain, (b) 2% compression strain, (c) 2% tensile strain, and (d) 6% tensile strain.

Published under license by AIP Publishing.

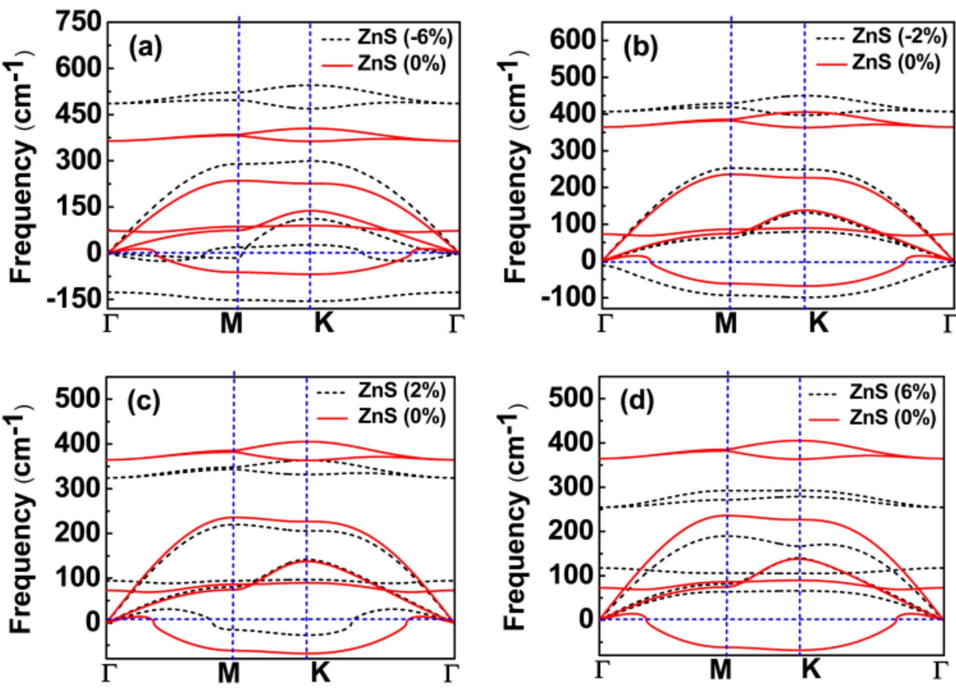

FIG. 11. Calculated phonon band dispersion of the ZnS monolayer: (a) 6% compression strain, (b) 2% compression strain, (c) 2% tensile strain, and (d) 6% tensile strain.

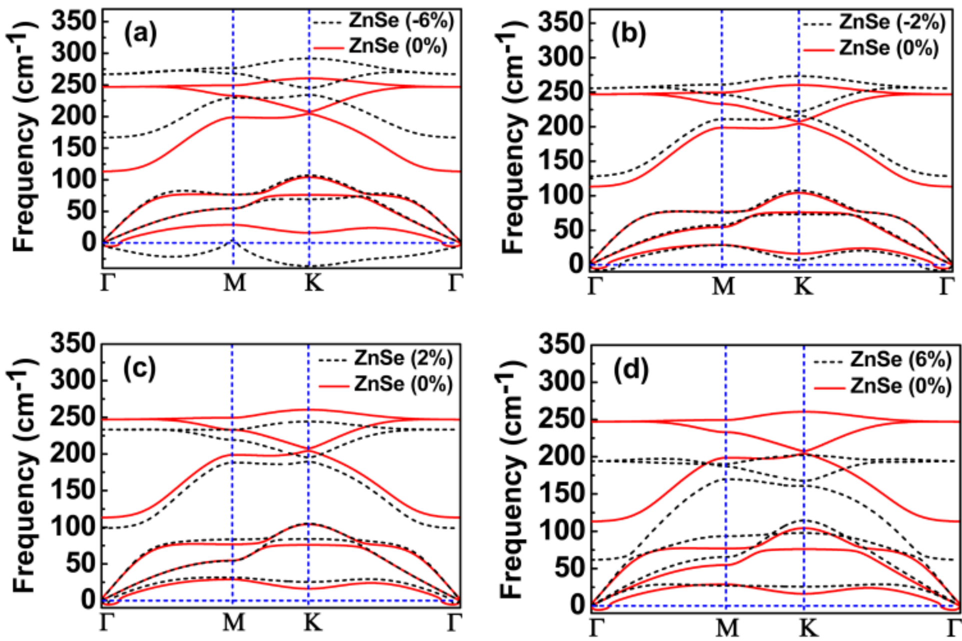

FIG. 12. Calculated phonon band dispersion of the ZnSe monolayer: (a) 6% compression strain, (b) 2% compression strain, (c) 2% tensile strain, and (d) 6% tensile strain.

Published under license by AIP Publishing.

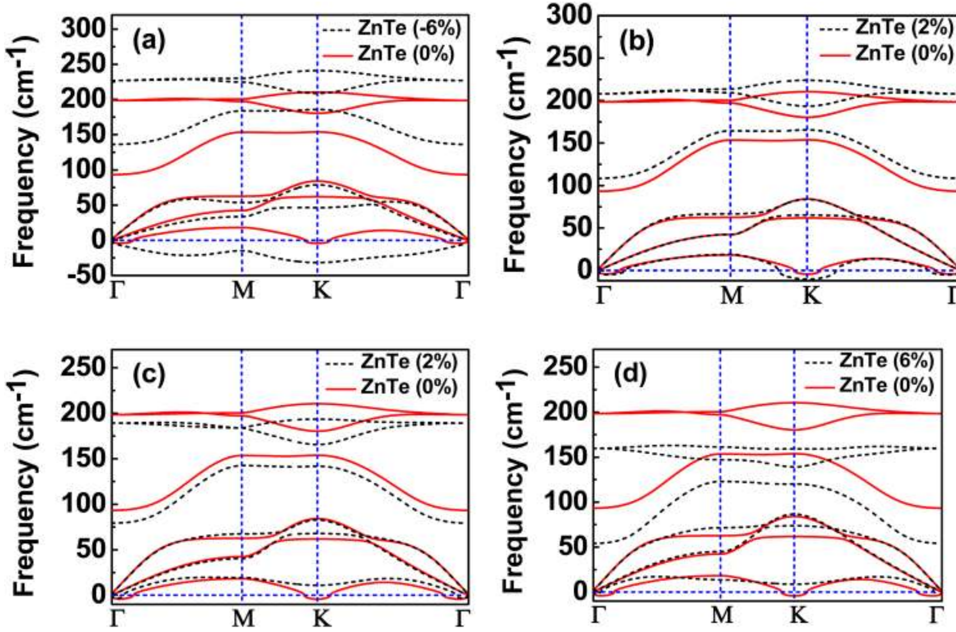

FIG. 13. Calculated phonon band dispersion of the ZnTe monolayer: (a) 6% compression strain, (b) 2% compression strain, (c) 2% tensile strain, and (d) 6% tensile strain.

All the modes of the ZnS phonon spectrum became positive at 4% of tensile strain, suggesting that the dynamically unstable phase becomes a dynamically stable ZnS monolayer at this tensile strain. Moreover, the ZA mode shows robustness with a further increase in the tensile strain, while the degenerate optical modes, LO/TO at Γ, M, and K follow a similar trend as in the ZnO monolayer under tensile and compressive strains.

The phonon spectra of buckled ZnSe and ZnTe monolayers at 2% and 6% are shown in Figs. 12 and 13, respectively, under compressive and tensile strains with pristine phonon spectra for these layers. The ZnSe monolayer phonon band dispersion is similar to the buckled silicene and germanene systems, studied by Yan *et al.*,[53] and ZnSe and ZnTe pristine monolayers show the small imaginary frequency ($<8\,cm^{-1}$) at Γ, and Γ and K, respectively. ZA out-of-plane phonon modes in these layers become softer, shifting toward lower imaginary frequencies with an increase in the compressive strain. Thus, the compressive strain increases the dynamic instability for these monolayers. The degenerate LO/TO optical modes at Γ shifted to higher frequencies with an increase in the compressive strain. The splitting of LO/TO modes at M showed a reduction with an increase in the compressive strain. The small imaginary frequency of pristine ZnSe and ZnTe monolayers shifted to the positive frequencies with even at 2% tensile strain, suggesting the transition from dynamically less stable to stable strained structures. The ZA mode shows robustness with an increase in the tensile strain for these monolayers, whereas the degenerate LO/TO optical modes at the Γ point are shifted to lower frequencies with an increase in the tensile strain, and splitting of LO/TO modes also showed enhancement in the frequency along Γ-M and Γ-K with an increase in the tensile strain.

The general condition for the stable structure in terms of lattice dynamics is that all phonon modes have real frequencies. An imaginary frequency of any of these modes leads the system to thermodynamical instability. However, it is well known that in the case of elastic materials like graphene and ZnX monolayers, the instability can occur from the softening of the acoustic branch at the zone center. Figure 14 shows the hardening or softening of the Raman active mode for ZnO, ZnS, ZnSe, and ZnTe monolayers under the compressive or tensile strain. Phonon mode hardening (compressive strain) of the Raman active mode E_{2g} and A_1 is relatively larger as compared to the phonon mode softening (tensile strain) in planar like ZnO and ZnS monolayers. Moreover, low buckled ZnSe and ZnTe monolayers exhibit opposite trends for phonon mode hardening or softening under the compressive or tensile strain as compared to planar ZnO and ZnS monolayers. Change in the frequency of Raman active modes of ZnO and ZnS monolayer as much higher as compared to low buckled ZnSe and ZnTe monolayers (Fig. 14).

C. Strain-modulated electronic properties

We considered biaxial compressive and tensile strain in −8% to 8% range at 1% interval to understand the change in electronic properties of ZnX monolayers. The computed VBM and CBM of electronic band structures are shown in Figs. 15 and 16 for compressive and tensile strains, respectively.

Published under license by AIP Publishing.

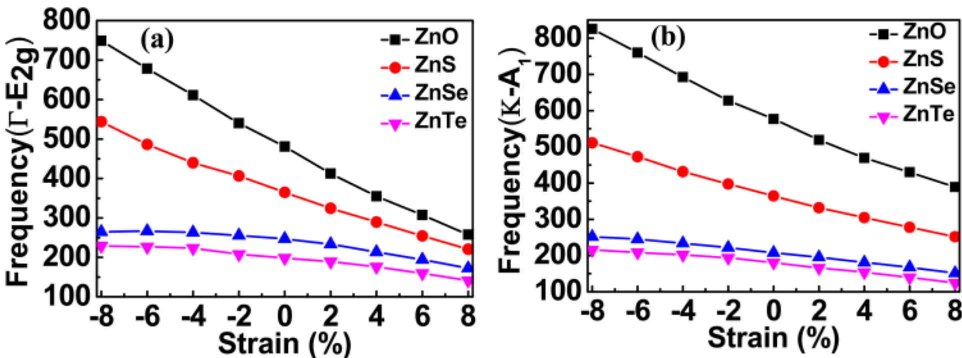

FIG. 14. Deviation of (a) E_{2g} and (b) A_1 as a function of applied biaxial strain of ZnX monolayers.

We notice that the CBM of ZnO and ZnS planar monolayers remain least affected [Figs. 15(a) and 15(b)], whereas the VBM is shifting lower in energy, i.e., far from the Fermi energy downwards under compressive strains [Figs. 15(a) and 15(b)]. Thus, the bandgap of ZnO and ZnS monolayers increases with an increase in the compression strain and the change is summarized in Fig. 17. The calculated maximum changes are 0.24 eV and 1.27 eV at Γ for ZnO and ZnS monolayers for −8% compressive strain with respect to the pristine structures. The bond lengths between the atoms reduce under compressive strains, causing enhanced orbital overlapping. This increased orbital overlapping is the main reason for the band reorganization away from the Fermi level. However, the nature of bandgap, i.e., the direct bandgap is conserved under the compressive strain for both ZnO and ZnS monolayers.

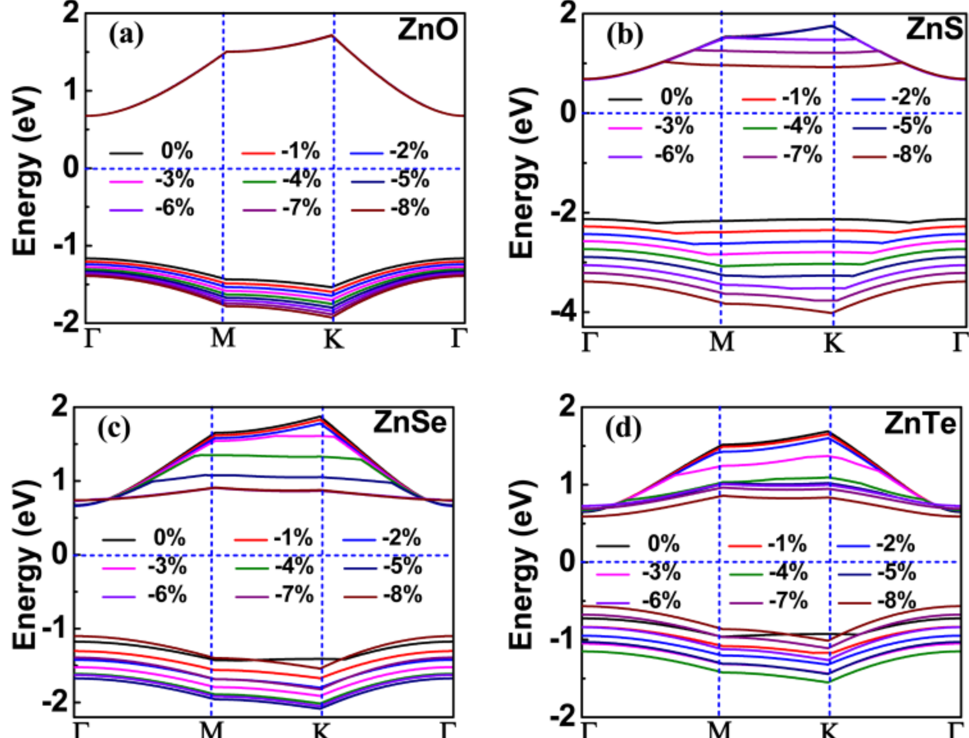

FIG. 15. Near band edge of (a) ZnO, (b) ZnS, (c) ZnSe, and (d) ZnTe under compressive strains.

Published under license by AIP Publishing.

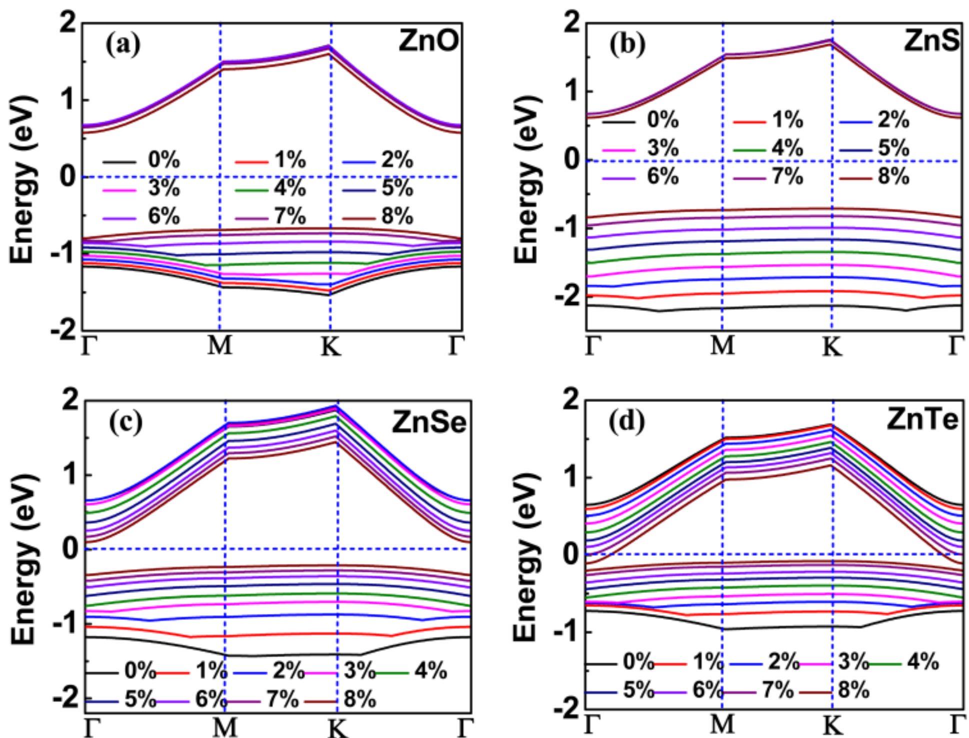

FIG. 16. Near band edge of (a) ZnO, (b) ZnS, (c) ZnSe, and (d) ZnTe under tensile strains.

In the case of the ZnSe monolayer, the CBM shows a small shift under the compressive strain, whereas the VBM shows a large shift and shifts away from the Fermi energy upto −6% compressive strain [Fig. 15(c)]. The VBM is shifted toward the Fermi energy with any further increase in the compressive strain, as shown in Fig. 15(c). Thus, the bandgap of the ZnSe monolayer increases upto −6% compressive strain and decreases at higher compressive strains. These changes are summarized in Fig. 17. The similar changes are predicted for the ZnTe monolayer against the compressive strain, where the bandgap increases upto −5% compressive strain and decreases afterwards. The maximum bandgap deviations are ~0.52 eV and ~0.38 eV at Γ for ZnSe and ZnTe monolayers, respectively. The nature of the bandgap, i.e., the direct bandgap is also conserved for ZnSe and ZnTe monolayers, similar to ZnO and ZnS monolayers against compressive strains.

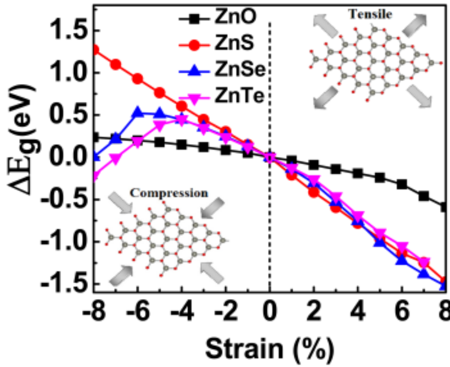

FIG. 17. Change in the bandgap as a function of applied biaxial strain with the inset showing the cartoons for tensile and compressive strains.

The changes in band structures are summarized in Fig. 16 for these monolayers under tensile strains (0%-8%). The CBM of ZnO and ZnS monolayers shows a small shift toward the Fermi energy, whereas the VBM shows a relatively large shift toward the Fermi energy. The VBM for the ZnO monolayer is located at Γ up to 5% tensile strain and is shifted to K with further increase in the tensile strain [Fig. 16(a)]. This suggests the onset of electronic phase transition (direct to indirect bandgap) at 6% of tensile strain for the ZnO monolayer. A similar electronic phase transition (direct to indirect bandgap) is observed at only 1% tensile strain for the ZnS monolayer. The maxima of valence band at 1% of tensile strain are shifted from Γ to K for ZnS monolayer, substantiating the indirect band behavior [Fig. 16(b)]. The observed changes in the bandgap of ZnS monolayers are summarized in Fig. 17.

The changes in the band structure for buckled ZnSe and ZnTe monolayers are shown in Figs. 16(c) and 16(d) under tensile strains. The CBM and VBM of ZnSe show a shift toward the Fermi energy [Fig. 16(c)], suggesting the reduction

Published under license by AIP Publishing.

in bandgap values with tensile strain. The VBM of the ZnSe monolayer is located at Γ up to 2% tensile stain and shifted to K with an increase in the tensile strain. This suggests the onset of the electronic phase transition (direct to indirect bandgap) at about 3% tensile strain in the ZnSe monolayer. The near band edge changes for the ZnTe monolayer under tensile strains are similar to that of the ZnSe monolayer [Fig. 16(d)]. The VBM and CBM in the ZnTe monolayer show a similar relative shifting like the ZnSe monolayer, moving toward the Fermi energy. The ZnTe monolayer also exhibits direct to indirect bandgap electronic phase transition at or above 2% tensile strains, where the VBM changed from Γ to K. The ZnTe monolayer showed another interesting indirect semiconductor to metal transition at 8% tensile strain, where the minima of conduction band crossed the Fermi energy. The changes in bandgap values for buckled ZnSe and ZnTe monolayers are illustrated in Fig. 17.

D. Strain-modulated carrier effective mass

The effective mass of charge carriers plays a vital role in affecting carrier mobilities in the materials. The effective masses of electron and hole are defined as $m^* = \hbar^2 \left[\frac{d^2E(k)}{d^2k}\right]^{-1}$, where m^* is the effective mass of the charge carrier; ħ is the reduced Plank constant; $E(k)$ is the energy band, and k is the reciprocal wave vector along the high symmetry direction. The carrier effective masses for pristine ZnX monolayers were discussed earlier and computed for different strained ZnX monolayers at Γ(0,0) and K(1/3, 1/3) under compressive and tensile strains. The variation of computed electron and hole effective masses against strain shown in Fig. 18 along (110) and (100) directions in the unit of m_e (m_e is the free mass of electron). The electron effective masses are 0.24 m_e, 0.16 m_e, 0.11 m_e, and 0.09 m_e and the hole effective masses are 1.00 m_e, 0.68m_e, 0.66 m_e, and 0.60m_e along (110) for pristine ZnO, ZnS, ZnSe, and ZnTe monolayers, respectively. The electron effective mass decreases linearly along (110) and (100) directions from compressive to tensile strains for ZnO and ZnS monolayers [Figs. 18(a) and 18(b)]. This slight variation in the electron effective mass is attributed to the observed change in the conduction band curvature at Γ(0,0) and K(1/3, 1/3) points (Figs. 15 and 16). The electron effective mass in ZnSe and ZnTe monolayers along (110) and (100) increases linearly from tensile strain to compressive strain, with a noticeable increase at −7% and −5% for ZnSe and ZnTe monolayers, respectively. The effective mass of electron in the ZnSe monolayer at −7% along the (110) direction significantly increases from 0.19 to 0.69m_e, while along (100) it increases from 0.19 to 0.99 m_e A similar behavior is also predicted for the ZnTe monolayer at −5% and the changes in the electron effective masses are 0.12 to 0.49m_e and 0.12 to 0.55m_e along (110) and (100) directions, respectively. Furthermore, with an increase in the compressive strain, the minima of

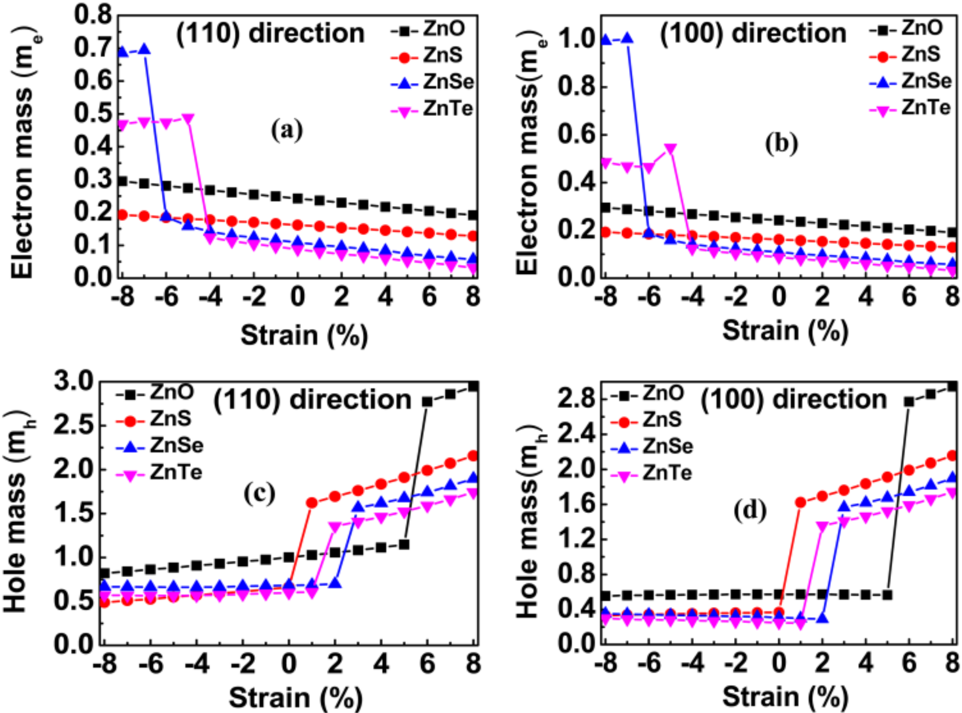

FIG. 18. Effective mass of (a) electron along (110), (b) electron along (100), (c) hole along (110), and (d) hole along (100) directions as a function of biaxial strain.

Published under license by AIP Publishing.

conduction band get flatter for ZnSe and ZnTe monolayers at Γ(0,0), as can be seen in Figs. 15(c) and 15(d).

The hole effective masses along (110) and (100) directions are almost constant under the compression strain for these ZnX monolayers. However, the relative change in the hole effective masses is observed near the direct to indirect bandgap under tensile strains. This increases linearly upto 5% tensile strain for the ZnO monolayer, followed by an increase from 0.56 to $2.94m_e$ along the (100) direction, where the direct to indirect bandgap is observed in the ZnO monolayer. This is attributed to the shift in the maxima of the valence band from Γ(0,0) to K(1/3, 1/3), where the curvature is more dispersive. The corresponding sudden variation in the hole effective mass is predicted at 1% tensile strain in the ZnS monolayer, where the hole effective mass increased from 0.37 to $1.62m_e$ and a further increase in the tensile strain showed a linear increase. Similar behaviors are predicted for ZnSe and ZnTe monolayers [Figs. 18(c) and 18(d)]. The increase in the hole effective mass is predicted at 3% and 2% tensile strains for ZnSe and ZnTe monolayers, respectively. This increases linearly with tensile strains above this point because of the change in the band slope at the K(1/3, 1/3) with tensile strains [Figs. 18(c) and 18(d)].

IV. SUMMARY

The effect of biaxial strain on the electronic and phonon properties of ZnX monolayers is investigated using the density functional theory. The structural stability is determined using phonon band dispersion. The calculated results find that the ZnO monolayer is dynamically robust, showing stability for −2% compressive strain as well as in conjunction with tensile strains. ZnS, ZnSe, and ZnTe are relatively less thermodynamically stable even under pristine conditions. Interestingly, ZnS, ZnSe, and ZnTe monolayers exhibited dynamic stability at 4%, 2%, and 2% biaxial tensile strains, respectively. The out-of-plane ZA acoustic mode is showing softening for the compressive strain, whereas it is relatively robust in the tensile strain. The buckling height of ZnSe and ZnTe monolayers is enhanced with an increase in the compressive strain, but is reduced under 8% tensile strain. The bandgap of ZnX monolayers is increased under compressive strains, but is reduced under tensile strains. ZnO, ZnS, and ZnSe monolayers show direct to indirect bandgap electronic transition under applied strains. The ZnTe monolayer shows not only direct to indirect electronic transitions at the intermediate strain values but also semiconducting to metallic transitions at the higher strain value. These transitions are accompanied by a sharp increase in the carrier effective masses. We believe that the predicted strain-induced properties of ZnX monolayers will be useful in the development of the next generation nanoscale devices.

SUPPLEMENTARY MATERIAL

The supplementary material includes the phonon band dispersions for different monolayers under compressive and tensile strains.

ACKNOWLEDGMENTS

Ambesh Dixit acknowledges the Department of Science and Technology, Government of India through Project No. DST/INT/Mexico/P-2/2016 for this work.

REFERENCES

[1]A. A. F. K. S. Novoselov, A. K. Geim, S. V. Morozov, D. Jiang, Y. Zhang, S. V. Dubonos, and I. V. Grigorieva, Science **306**, 666 (2004).
[2]S. Chen, Q. Wu, C. Mishra, J. Kang, H. Zhang, K. Cho, W. Cai, A. A. Balandin, and R. S. Ruoff, Nat. Mater. **11**, 203 (2012).
[3]K. I. Bolotin, K. J. Sikes, Z. Jiang, M. Klima, G. Fudenberg, J. Hone, P. Kim, and H. L. Stormer, Solid State Commun. **146**, 351 (2008).
[4]C. Lee, X. Wei, J.W. Kysar, and J. Hone, Science **321**, 385 (2008).
[5]M. A. Worsley, P. J. Pauzauskie, T. Y. Olson, J. Biener, J. H. Satcher, and T. F. Baumann, J. Am. Chem. Soc. **132**, 14067 (2010).
[6]K. S. Novoselov, A. K. Geim, S. V. Morozov, D. Jiang, M. I. Katsnelson, I. V. Grigorieva, S. V. Dubonos, and A. A. Firsov, Nature **438**, 197 (2005).
[7]M. Chhowalla, H. S. Shin, G. Eda, L.-J. Li, K. P. Loh, and H. Zhang, Nat. Chem. **5**, 263 (2013).
[8]H. Şahin, S. Cahangirov, M. Topsakal, E. Bekaroglu, E. Akturk, R. T. Senger, and S. Ciraci, Phys. Rev. B **80**, 1 (2009).
[9]H. Zheng, X. Bin Li, N. K. Chen, S. Y. Xie, W. Q. Tian, Y. Chen, H. Xia, S. B. Zhang, and H. B. Sun, Phys. Rev. B **92**, 115307 (2015).
[10]W. Choi, N. Choudhary, G. H. Han, J. Park, D. Akinwande, and Y. H. Lee, Mater. Today **20**, 116 (2017).
[11]R. K. Swank, Phys. Rev. **153**, 844 (1967).
[12]S. Mokkapati and C. Jagadish, Mater. Today **12**, 22 (2009).
[13]I. Vurgaftman, J. R. Meyer, and L. R. Ram-Mohan, J. Appl. Phys. **89**, 5815 (2001).
[14]S. Adachi, *Properties of Group-IV, III-V and II-VI Semiconductors* (John Wiley and Sons, Ltd, Publication, 2009).
[15]C. Tusche, H. L. Meyerheim, and J. Kirschner, Phys. Rev. Lett. **99**, 2 (2007).
[16]T. Sahoo, S. K. Nayak, P. Chelliah, M. K. Rath, and B. Parida, Mater. Res. Bull. **75**, 134 (2016).
[17]J. H. Kim, M. Jin, Y. C. Jun, R. Erni, S. K. Kwak, and J. Yoo, Nano Lett. **17**, 120 (2016).
[18]S.H. Yu and M. Yoshimura, Adv. Mater. **14**, 296 (2012).
[19]Y. H. Zhang, M. L. Zhang, Y. C. Zhou, J. H. Zhao, S. M. Fang, and F. Li, J. Mater. Chem. A **12**, 13129 (2014).
[20]J. Lei, M. C. Xu, and S. J. Hu, J. Appl. Phys. **118**, 104302 (2015).
[21]H. Guo, Y. Zhao, N. Lu, E. Kan, X. C. Zeng, X. Wu, and J. Yang, J. Phys. Chem. C **116**, 11336 (2012).
[22]C. Tan, D. Sun, D. Xu, X. Tian, and Y. Huang, Ceram. Int. **42**, 10997 (2016).
[23]G. S. Rao, T. Hussain, M. S. Islam, M. Sagynbaeva, D. Gupta, P. Panigrahi, and R. Ahuja, Nanotechnology **27**, 015502 (2016).
[24]H. Lashgari, A. Boochani, A. Shekaari, S. Solaymani, E. Sartipi, and R. T. Mendi, Appl. Surf. Sci. **369**, 76 (2016).
[25]Q. Peng, L. Han, X. Wen, S. Liu, Z. Chen, J. Lian, and S. De, RSC Adv. **5**, 11240 (2015).
[26]M. Shahrokhi, Appl. Surf. Sci. **390**, 377 (2016).
[27]L. Li, P. Li, N. Lu, J. Dai, and X. C. Zeng, Adv. Sci. **2**, 1500290 (2015).
[28]J. Zhou and X. Wu, Mater. Today Chem. **4**, 40 (2017).
[29]J. Zhou, Y. Li, X. Wu, and W. Qin, ChemPhysChem **17**, 1 (2016).
[30]X. H. Huang, Z. Y. Zhan, K. P. Pramoda, C. Zhang, L. X. Zheng, and S. J. Chua, CrystEngComm **14**, 5163 (2012).
[31]B. Wei, K. Zheng, Y. Ji, Y. Zhang, Z. Zhang, and X. Han, Nano Lett. **12**, 4595 (2012).
[32]K. J. Lee, L. M. Browning, P. D. Nallathamby, C. J. Osgood, and X. H. N. Xu, Nanoscale **5**, 11625 (2013).
[33]P. Johari and V. B. Shenoy, ACS Nano **6**, 5449 (2012).
[34]K. S. Kim, Y. Zhao, H. Jang, S. Y. Lee, J. M. Kim, K. S. Kim, J. H. Ahn, P. Kim, J. Y. Choi, and B. H. Hong, Nature **457**, 706 (2009).
[35]G. Cocco, E. Cadelano, and L. Colombo, Phys. Rev. B **81**, 1 (2010).

Published under license by AIP Publishing.

[36]H. Behera and G. Mukhopadhyay, Phys. Lett. A **376**, 3287 (2012).
[37]H. Behera and G. Mukhopadhyay, e-print arXiv:1210.3309 (2012).
[38]Z. H. Ni, T. Yu, Y. H. Lu, Y. Y. Wang, Y. P. Feng, and Z. X. Shen, ACS Nano **2**, 2301 (2008).
[39]R. Yang, J. Lee, S. Ghosh, H. Tang, R. M. Sankaran, C. A. Zorman, and P. X. Feng, Nano Lett. **17**, 4568 (2017).
[40]V. Lacivita, A. Erba, Y. Noël, R. Orlando, P. D'Arco, and R. Dovesi, J. Chem. Phys. **138**, 214706 (2013).
[41]R.M. Dreizler, *Density Functional Theory* (Springer, 1990).
[42]P. Ordejon, E. Artacho, and J. Soler, Phys. Rev. B **53**, R10441 (1996).
[43]D. Sánchez-Portal, P. Ordejón, E. Artacho, and J. M. Soler, Int. J. Quantum Chem. **65**, 453 (1997).
[44]J. M. Soler, E. Artacho, J. D. Gale, A. García, J. Junquera, P. Ordejón, and D. Sánchez-Portal, J. Phys. Condens. Matter **2745**, 2745 (2002).
[45]P. W. Tasker, Phys. Rev. Lett. **77**, 3865 (1996).
[46]G. B. Bachelet, D. R. Hamann, and M. SchÌter, Phys. Rev. B **26**, 4199 (1982).
[47]S. Baroni, S. De Gironcoli, A. Dal Corso, and P. Giannozzi, Rev. Mod. Phys. **73**, 515 (2001).
[48]P. Giannozzi, S. Baroni, N. Bonini, M. Calandra, R. Car, C. Cavazzoni, D. Ceresoli, G. L. Chiarotti, M. Cococcioni, I. Dabo, A. Dal Corso, S. De Gironcoli, S. Fabris, G. Fratesi, R. Gebauer, U. Gerstmann, C. Gougoussis, A. Kokalj, M. Lazzeri, L. Martin-Samos, N. Marzari, F. Mauri, R. Mazzarello, S. Paolini, A. Pasquarello, L. Paulatto, C. Sbraccia, S. Scandolo, G. Sclauzero, A. P. Seitsonen, A. Smogunov, P. Umari, and R. M. Wentzcovitch, J. Phys. Condens. Matter **21**, 1 (2009).
[49]H. J. Monkhorst and J. D. Pack, Phys. Rev. B **13**, 5188 (1976).
[50]H. Nejatipour and M. Dadsetani, J. Electron Spectros. Relat. Phenomena **203**, 14 (2015).
[51]M. Safari, Z. Izadi, J. Jalilian, I. Ahmad, and S. Jalali-Asadabadi, Phys. Lett. A **381**, 663 (2017).
[52]J. Maultzsch, S. Reich, C. Thomsen, H. Requardt, and P. Ordejón, Phys. Rev. Lett. **92**, 075501 (2004).
[53]J. Yan, S. Gao, R. Stein, and G. Coard, Phys. Rev. B **91**, 245403 (2015).
[54]H. K. Hong, J. Jo, D. Hwang, J. Lee, N. Yeon, S. Son, J. H. Kim, M. J. Jin, Y. C. Jun, R. Erni, S. K. Kwak, J. W. Yoo, and Z. Lee, Nano Lett. **17**, 120 (2017).
[55]C. Yang, Z. Yu, P. Lu, Y. Liu, H. Ye, and T. Gao, Comput. Mater. Sci. **95**, 420 (2014).
[56]T. Hu, Y. Han, and J. Dong, Nanotechnology **25**, 455703 (2014).
[57]Q. Peng and S. De, Phys. Chem. Chem. Phys. **15**, 19427 (2013).
[58]H. Wang, Q. Li, Y. Gao, F. Miao, and X. Zhou, New J. Phys. **18**, 073016 (2016).
[59]T. P. Kaloni and U. Schwingenschlögl, Chem. Phys. Lett. **583**, 137 (2013).
[60]B. Sa, Y. Li, J. Qi, R. Ahuja, and Z. Sun, J. Phys. Chem. C **118**, 26560 (2014).
[61]P. K. Jha and H. R. Soni, J. Appl. Phys. **115**, 023509 (2014).

Published under license by AIP Publishing.